Check for updates

Development of a 3D printed perfusable *in vitro* blood−brain barrier model for use as a scalable screening tool†

Madison K. Royse,‡[a] Martha Fowler,‡[a] A. Kristen Mai, [ID][a] Yufang He, [ID][b] Marc R. Durante,[b] Nicole Buist,[c] Adam Procopio,[c] Jun Xu [ID] *[c] and Omid Veiseh [ID] *[a]

Despite recent technological advances in drug discovery, the success rate for neurotherapeutics remains alarmingly low compared to treatments for other areas of the body. One of the biggest challenges for delivering therapeutics to the central nervous system (CNS) is the presence of the blood−brain barrier (BBB). *In vitro* blood−brain barrier models with high predictability are essential to aid in designing parameters for new therapeutics, assess their ability to cross the BBB, and investigate therapeutic strategies that can be employed to enhance transport. Here, we demonstrate the development of a 3D printable hydrogel blood−brain barrier model that mimics the cellular composition and structure of the blood−brain barrier with human brain endothelial cells lining the surface, pericytes in direct contact with the endothelial cells on the abluminal side of the endothelium, and astrocytes in the surrounding printed bulk matrix. We introduce a simple, static printed hemi-cylinder model to determine design parameters such as media selection, co-culture ratios, and cell incorporation timing in a resource-conservative and high-throughput manner. Presence of cellular adhesion junction, VE-Cadherin, efflux transporters, P-glycoprotein (P-gp) and Breast cancer resistance protein (BCRP), and receptor-mediated transporters, Transferrin receptor (TfR) and low-density lipoprotein receptor-related protein 1 (LRP1) were confirmed *via* immunostaining demonstrating the ability of this model for screening in therapeutic strategies that rely on these transport systems. Design parameters determined in the hemi-cylinder model were translated to a more complex, perfusable vessel model to demonstrate its utility for determining barrier function and assessing permeability to model therapeutic compounds. This 3D-printed blood−brain barrier model represents one of the first uses of projection stereolithography to fabricate a perfusable blood−brain barrier model, enabling the patterning of complex vessel geometries and precise arrangement of cell populations. This model demonstrates potential as a new platform to investigate the delivery of neurotherapeutic compounds and drug delivery strategies through the blood−brain barrier, providing a useful *in vitro* screening tool in central nervous system drug discovery and development.

Introduction

The neurovascular unit (NVU) contains blood–brain barrier capillaries, neurons, and supporting cells in the brain stroma (such as microglia, macrophages, and other glial cells) and their basement membrane.[1] One crucial part of the neurovas-cular unit is the blood–brain barrier. The blood–brain barrier (BBB) is a structural and metabolic barrier that separates the bloodstream from the central nervous system (CNS). The BBB is essential for protecting the brain and maintaining homeo-stasis in the CNS. The main cellular components of this barrier are non-fenestrated brain microvascular endothelial cells, pericytes, and astrocytes. The pericytes are in direct contact with the endothelial cells and ensheathe the endo-thelial lining to mediate the contraction of the endothelial wall. Astrocytes reside in the surrounding extracellular matrix and have end-feet projections that almost entirely encase the vessels of endothelial cells and pericytes. From there, astro-cytes can regulate blood flow and help maintain the BBB. Each of these cells' unique features is imperative for the proper function of the blood–brain barrier.[2,3]

[a]Department of Bioengineering, Rice University, 6100 Main St., Houston, TX 77005, USA. E-mail: omid.veiseh@rice.edu
[b]Division of Technology, Infrastructure, Operations & Experience, Merck & Co., Inc. Rahway, NJ 07065, USA
[c]Department of Pharmaceutical Sciences & Clinical Supply, Merck & Co., Inc. Rahway, NJ 07065, USA. E-mail: jun.xu8@merck.com

†Electronic supplementary information (ESI) available. See DOI: https://doi.org/10.1039/d4bm00663a
‡These authors contributed to the work equally.

Historically, studies for drug development of neuro pharmaceuticals have been assessed using both *in vivo* and *in vitro* methods. *In vivo* methods using animals are beneficial in recapitulating biological complexities and are generally regarded as the gold standard for preclinical validation of therapies in development,[4] however, species differences between animal and human systems, such as genetic differences and lifespan, may produce results that fail to predict complications or proper efficacy in humans.[5] It has been reported that more than 80% of candidate drugs deemed successful in animal models failed in clinical trials.[6] Additionally, animal models are costly, labor-intensive, and are facing increasing pressure due to ethical issues associated with their use.[7] As a result, there has been a shift towards developing enhanced *in vitro* models that incorporate more biological intricacies and can better replicate the human *in vivo* environment for more accurate prediction of therapeutic outcomes. Additionally, there has been recent legislation passed to push the field towards utilizing the increasingly more accurate *in vitro* models being developed. In December 2022, the FDA Modernization Act 2.0 was signed into law. This law eliminated the requirement that all drugs developed for humans must first be tested on animals. This legislation encourages the use of alternative testing strategies such as organ-on-a-chip and other *in vitro* models that enable the assessment of drug safety, thus reducing the number of animal studies performed.[8]

The first *in vitro* technologies relied on 2D cell culture for drug discovery. Models consisting of a single layer of cells grown in the lab are robust, reproducible, and easy to analyze. These models may prove helpful in assessing the cytotoxicity of a drug candidate, as well as an initial assessment of drug efficacy. However, the 2D models are limited and often cannot recapitulate crucial complexities within a physiological setting, such as fluid shear stress mechanical stimulation and interactions with neighboring cells and the extracellular matrix in a 3D environment. These factors are essential for influencing cell function, signaling pathways, stimuli response, and gene and protein expression – all crucial components for the accurate prediction of human drug response.[9] Therefore, there is a need for an *in vitro* system that can model more complex systems to enable the screening of therapeutic compounds in a more representative environment.

For more complex, 3D, *in vitro* models, one of the leading technologies in this area is the organ-on-a-chip platform. Organs-on-chips are microfluidic *in vitro* cell culture systems that recapitulate the functions of human organs. These microfluidic devices are populated with relevant cell types in hollow 3D channels and can be cultured under perfusion to form cell layers. These models show potential for disease modeling and high-throughput drug screening to assess the physiologic response of human tissues or organs.[10] The first organ-on-a-chip platform was focused on lung function and published in 2010,[11] and since then, much effort has been focused on extending the platform to replicate other organs of the body, such as the heart, intestine, kidney, and liver.[12]

Given the challenges in drug discovery regarding neuropharmaceuticals, there has been significant interest in extending the organ-on-a-chip technology toward recapitulating the BBB. Microfluidics/organ-on-a-chip devices are one of the most prevalent technologies to assess BBB function. One of the most used microfluidic BBB chips is the commercially available OrganoPlate manufactured by Mimetas. It has been adapted to create a BBB model through the incorporation of brain endothelial cells, pericytes, and astrocytes.[13] While the OrganoPlate is a high throughput and enables shear stress compared to traditional models, it has a few notable limitations. Perfusion in the OrganoPlate is planar and occurs *via* rocking, which is sub-optimal, mimicking *in vivo* conditions. Contrary to steady flow, oscillatory flow has the potential to disrupt cell–cell junctions and fails to induce cytoskeletal remodeling typically associated with flow conditions.[14] Additionally, limitations associated with microfluidics include a technically complex fabrication procedure that makes it difficult to iterate through various architectural designs and a lack of cell–cell contacts, an essential component for recreating the blood–brain barrier in an *in vitro* model.

In addition to 2D cell monolayers and microfluidic chips, additional platforms have arisen as potential BBB model alternatives. Some of these include spheroids, self-assembled microvasculature, vessel-like structures in gels, and bioprinted models.[15–21] For the BBB models generated *via* bioprinting, two-photon lithography has been used to fabricate a microfluidic system with cylindrical, porous microcapillaries, and another group has demonstrated a PCL/PLGA microfluidic perfusion system manufactured by freeze-coating a 3D-printed sacrificial template.[22,23] The use of 3D bioprinting for fabricating a BBB model holds immense potential for reducing the manufacturing difficulties associated with traditional microfluidics, enabling tunable perfusion and shear stress, permitting real-time visualization of cell morphology and fabricating complex geometries that allow for the precise placement of cell types. Utilizing 3D projection stereolithography printing, we have recently demonstrated a novel 3D bioprinted perfusable vessel-mimicking hydrogel as a scalable platform for delivery of therapeutics across a cellular barrier.[24]

This work applies our 3D bioprinted platform to investigate fabrication methods for innovative and novel BBB models with anatomically relevant cell populations and structural organization for utilization as a scalable screening tool in drug development. A static 2.5D hemi-cylinder hydrogel model, that is easily tunable, was first fabricated for optimization of BBB conditions such as culture media selection, co-culture ratio, cell incorporation order, and culture durations. The 2.5D model demonstrated human brain endothelial cells in direct contact with pericytes, and astrocytes in the surrounding printed matrix which displayed key cellular adhesion junctions as previously demonstrated with general endothelial cells[24] and relevant transporters. These optimized parameters were then extended to a 3D perfusable channel model to validate the model's potential for assessing barrier function to model compounds. Finally, this 3D BBB model was subjected to an ultra-

sound therapeutic to demonstrate this model's capability as a 3D BBB platform. These 3D bioprinted hydrogels model uniquely provides an *in vitro* platform to inform future design and screening of neurotherapeutics.

Experimental section

3D printing of hydrogels

The polymers and initiators for the pre-hydrogel solutions, including poly(ethylene glycol) diacrylate (PEGDA; 3.4 kDa), lithium phenyl-2,4,6-trimethylbenzoylphosphinate (LAP), gelatin methacrylate (GelMA) were synthesized as previously described.[25] Fabrication of the 3D-printed hydrogels was conducted as previously described.[25,26] Briefly, pre-hydrogel mixtures contained 10 wt% GelMA, 3.25 wt% 3.4 kDa PEGDA, 17 mM LAP, 2.255 mM tartrazine photo absorber, and 10% glycerol in sterile 1× PBS. Hydrogel printing was conducted on the Lumen Bioprinter previously developed in the Miller lab.[25,26]

Printing astrocyte-containing hydrogel half pipes

The fabrication of cellular monolithic gels, pre-hydrogel mixtures were prepared according to the same formula listed above.[26] Immediately before printing, human brain astrocytes (HBAs) from (passages 5–7, AngioProteomie, cAP-0031) were resuspended in the pre-hydrogel mixture at a concentration of 6×10^6 cells per mL. This concentration was selected based on unpublished lab work demonstrating the ability to print at this density of cells in bulk without needing print parameter modification. Additionally, all cells were cultured and passaged upon reaching confluence in p1000 tissue dishes with Astrocytes Growth Medium (AGM, contains FBS and Growth factor supplements, cAP-29) supplemented with 1% penicillin/streptomycin (Sigma-Aldrich P4333). To passage, cells are removed from tissue culture dishes with 0.25% trypsin-EDTA (Gibco, #25200056) and incubated at 37 °C and 5% CO_2 for 3–5 minutes. AGM media was then added at equal amounts of trypsin to neutralize trypsin and centrifuged at 500*g* for 5 minutes. The pellet is collected and resuspended in AGM media at 1×10^6 cells per mL and cultured onto p1000 tissue culture dishes.

This 2.5D model of a hydrogel half pipe was created in Blender and designed with flat and curved hemispherical surfaces surrounded by 1 mm tall hydrogel walls that hold a volume of ~50 μL of solution. After printing, the 2.5D half pipe is removed from the glass slide of the build platform with a sterile razor and equilibrated in complete AGM media. Multiple AGM media washes are performed to remove any unreacted moieties.

Pericyte seeding on the astrocyte-containing hydrogel half pipes

The HBA-containing hydrogel half-pipes were soaked in AGM media overnight in individual wells of a 24-well plate. Red fluorescent protein labeled human brain microvascular pericytes (RFP-HBMPs) (passages 5–7, AngioProteomie, cAP-0030RFP)

were resuspended and seeded onto the hydrogel surface at 0.4×10^6 cells per cm^2 and left for 4 hours at 37 °C. After seeding, the gels were covered with 1 mL of complete Pericyte Growth Medium (PGM, contains FBS and Growth factor supplements, cAP-09). RFP-HBMPs were cultured on the HBA-containing hydrogel half pipes for three days before the addition of endothelial cells. Media changes were conducted daily using PGM media supplemented with 1% penicillin/streptomycin. Images were acquired daily on Nikon Ti epifluorescent microscope at 4×, 10×, or 20× magnification.

Endothelial cell seeding on pericyte and astrocyte-containing half pipes

After three days of pericyte culture, GFP-expressing human brain microvascular endothelial cells (GFP-HBMECs) (passages 5–7, AngioProteomie, cAP-0002GFP) were seeded on the HBA and RFP HBMP-containing hydrogel half pipe. GFP-HBMECs were resuspended from freeze and pipetted onto the pericyte-filled hydrogel surface at 0.4×10^6 cells per cm^2, creating a 1 : 1 ratio of pericytes to endothelial cells on top of the astrocyte-containing printed half pipe. To enable HBMEC adhesion, the half pipes were seeded for 4 hours at 37 °C. After seeding, the gels were covered with 1 mL of complete Vasculife (Endothelial medium complete kit, LifeLine, LL-0003) media supplemented with 1% penicillin/streptomycin rather than gentamicin, the tri-culture hydrogel was established. These tri-culture half pipes were carried out for six days (for a total culture time of ten days for the HBAs printed in bulk, nine days for the RFP-HBMPs seeded on top of the hydrogel, and six days for the GFP-HBMECs seeded on top). Media changes were conducted daily using Vasculife media supplemented with 1% penicillin/streptomycin. Images were acquired daily on Nikon Ti epifluorescent microscope at 4×, 10×, or 20× magnification.

Immunostaining of VE-Cadherin and BBB transporters on tri-culture hydrogel half pipes

Tri-culture hydrogel half-pipes were cultured with complete Vasculife media supplemented with 1% penicillin/streptomycin for six (6) days after adding the final cell type, GFP-HBMECs. For the following staining steps, 50 μL of each solution per hydrogel was pipetted onto the surface sequentially, being careful not to puncture the hydrogel with the pipette tip. First, the cell monolayers were fixed with 4 wt% paraformaldehyde (PFA, Thermo Scientific, AAJ6189) and allowed to soak for 10 minutes at RT, followed by 20 minutes of permeabilization with 0.1% Triton X-100 (Sigma-Aldrich, X100) in PBS. Then cells were blocked with 1 wt% bovine serum albumin (BSA, Sigma-Aldrich, A9418) for 1 hour at RT. The primary antibody for VE-cadherin (VE-Cadherin, D87F2 Rabbit mAb, Cell Signaling Technology) was prepared at 1 : 400 in 1 wt% BSA solution, and 50 μL pipetted onto each gel to incubate overnight at 4 °C. Transporters were stained for using primary antibodies for P-glycoprotein 1 (P-gp) (Rabbit polyclonal to P glycoprotein, Abcam, ab235954), breast cancer resistance protein (BCRP) (Rabbit monoclonal to BCRP/ABCG2, Abcam, ab229193), transferrin receptor (TfR) (Rabbit mono-

clonal to the transferrin receptor, Abcam, ab214039), and low-density lipoprotein receptor-related protein 1 (LRP1) (LRP1, Rabbit mAb #26387, Cell Signaling Technology). Primary antibodies were prepared at 1 : 50 in 1 wt% BSA solution and 50 μL pipetted onto each gel to incubate overnight at 4 °C. Following overnight incubation, 3 × 30 min washes with PBS were done before incubating with the secondary antibody (Anti-rabbit IgG (H + L) #4414, Alexa Fluor® 647 Conjugate, Cell Signaling Technology) prepared at a 1 : 500 dilution for 2 hours. A nuclear counter-stain was applied using 2.5 μg mL^{-1} Hoechst for 15 minutes. Finally, all gels were washed for 3 × 30 minutes with PBS before imaging. Images were acquired on Nikon A1-Rsi Confocal at 10× magnification.

Printing of astrocyte-containing 3D hydrogels

Identical to the 2.5D studies, before printing, human brain astrocytes (HBAs) (passages 5–7, AngioProteomie, cAP-0030) were resuspended in the pre-hydrogel mixture at a concentration of 6×10^6 cells per mL. The HBA-containing 3D straight channel hydrogels were soaked in complete Vasculife media supplemented with 1% penicillin/streptomycin overnight in individual wells of a 6-well plate. Multiple Vasculife media washes are performed to remove any unreacted moieties.

Seeding pericytes then endothelial cells into the channel of the astrocyte-containing hydrogels

The 3D printed hydrogels containing 6×10^6 cells per mL HBAs printed into the bulk and a 700 μm diameter channel were transferred into sterilized 3D printed plastic housing chambers with aligned ports for fluidic tips. Fluidic tips were primed with media and gently inserted into the gel chamber and then into the inlet and outlet portions of the hydrogel. RFP HBMPs were resuspended from freeze to a density of 30×10^6 cells per mL for seeding and injected into the channel. Gels were seeded for 4 hours at 37 °C and rotated 90 degrees every 15 minutes. After seeding, gels were perfused with complete Vasculife media supplemented with 1% penicillin/streptomycin at a flow rate of 5 μL min^{-1}. Pericytes were cultured under flow within the channel of the HBA-containing printed gel for one to three days (see timeline studies in the results) before endothelial cell inclusion.

After one to three days of pericyte culture, GFP-expressing human brain microvascular endothelial cells (GFP-HBMECs) (passages 5–7, AngioProteomie, cAP-0002GFP) were seeded within the channel of the HBA and RFP HBMP-containing 3D straight channel hydrogel. GFP-HBMECs were seeded at 30×10^6 cells per mL, matching the 1 : 1 ratio of endothelial cells to pericytes optimized in the 2.5D half-pipe studies. Gels were seeded for 4 hours at 37 °C and rotated 90 degrees every 15 minutes. After seeding, gels were perfused with complete Vasculife media supplemented with 1% penicillin/streptomycin at a flow rate of 5 μL min^{-1}. After the addition of the GFP-HBMECs, the tri-culture hydrogel half pipes were carried out for three to six days (for a total culture time of ten days for the HBAs printed in bulk, nine days for the RFP HBMPs seeded on top of the hydrogel, and six days for the GFP

HBMECs seeded on top), mimicking the timeline used in the 2.5D studies. Images were acquired daily on Nikon Ti epifluorescent microscope at 4×, 10×, or 20× magnification.

Demonstration of therapeutic screening studies

The 3D-printed cellular hydrogels were perfused with Vasculife media for three days at 5 μL min^{-1}. These hydrogels were subjected to an ultrasound-based permeability assay with intraluminal microbubble administration through the open channels of the 3D-printed hydrogels as previously established.[28] In the absence of cells and for the HBA only hydrogels, the hydrogels were perfused with 150 kDa FITC-dextran (Sigma-Aldrich, FD150S) to define the hydrogel channel barrier as previously described.[28] The higher molecular weight FITC-dextran was perfused to fill the channel so that the edge-detection feature of the custom GUI could be utilized. All hydrogels were perfused with Donkey Anti-Rabbit IgG (ab10755, Alexa Fluor® 555, Abcam) as the channel perfusate at a constant flow rate of 100 μL min$^-$ and were imaged in real-time using an epifluorescent microscope (Nikon). A 3D-printed cassette was customized to accommodate the perfusate and ultrasound catheterization. The ultrasound transducer probe was secured to the top of the printed hydrogels with ultrasound conductive gel between the probe and hydrogel. An imaging acquisition was set up to image fluorescent IgG permeability in real time over a twenty-minute time loop. Ultrasound was activated after ten minutes into the acquisition and applied at 2.0 W cm^{-2}, 1 MHz frequency, and 50% duty cycle for five minutes. The middle hydrogel channel was selected as the region of interest (ROI) during the image acquisition. Following ultrasound, the permeability coefficient was assessed with a customized MatLab GUI that tracks and quantifies the fluorescent intensities of the perfusate and endothelial cell barrier within the hydrogel. For acellular and astrocyte-only hydrogels, the acquisition did not start until the perfusate could be detected within the channels to ensure similarities in the acquisition starting point between astrocyte-only hydrogels and endothelialized hydrogels.

Calculation of permeability coefficient

To perform the permeability and ultrasound studies, the hydrogel remaining in its sterile chamber was removed from incubation and media perfusion to be transferred to a Nikon Eclipse Ti inverted epifluorescence microscope (Nikon Instruments Inc.) with a Zyla 4.2 sCMOS camera (Andor) to acquire time-lapsed imaging during the perfusion of a fluorescent compound with microbubbles.

These permeability ultrasound studies were conducted with a continuous perfusate flow of 100 μL min^{-1} throughout the entire time-lapsed acquisition. The flow of the perfusate was initiated, and at the 10 minute mark, ultrasound with a frequency of 1 MHz, duty cycle of 50%, and power of 2.0 W cm^{-2} was applied to the hydrogel for 5 minutes. Each trial consisted of perfusate flow and image acquisition for 10 minutes to allow equilibration, 5 minutes for ultrasound application, and 5 minutes after ultrasound application, for a total of 20 minute trials. Time-lapsed acquisitions of the fluorescent

molecule channel were used to calculate the apparent permeability coefficient with the equation below,

$$P = \frac{dI}{dt}\frac{r}{2I_0}$$

where P is the apparent permeability coefficient, dI/dt is the change in fluorescence intensity of the dye over time, r is the radius of the endothelialized channel, and I_0 is the maximum fluorescence intensity inside the lumen. The change in fluorescence intensity (dI/dt) was determined by monitoring a region outside the channel at a fixed distance from the channel edge and the maximum fluorescence intensity (I_0) was determined by the fluorescence intensity of the dye within the lumen at a time before the diffusion of the dye out of the gel occurs. The image processing used to determine each of these variables is described in previous work.[25]

For each trial, a permeability coefficient was calculated before and after the ultrasound to assess the effects of ultrasound on permeability and barrier function. The permeability coefficient before the ultrasound was determined using the 5 minutes before the ultrasound was applied. The permeability coefficient after ultrasound was determined using the 5 minutes after the ultrasound ended.

Statistical analysis

A paired t-test was used for statistical analysis to evaluate the permeability coefficients before and after ultrasound for the perfusion-based permeability studies, $*P < 0.05$, $**P < 0.01$, $***P < 0.001$, and $****P < 0.0001$. All statistical analyses were performed using the GraphPad Prism software package (PRISM 9.3.0; GraphPad Software). Biological replicates were used in all experiments unless otherwise stated. All experimental results were indicated as the mean ± SD unless otherwise specified.

Results and discussion

Development of a blood–brain barrier tri-culture model

A 2.5D static culture model was designed with a half-pipe architecture to screen cell parameters for BBB tri-culture. Both static half-pipe hydrogels and 3D-printed serpentine channel hydrogels were printed with HBMAs in the bulk of the hydrogel (Fig. 1 and ESI Fig. 1†). HBMPs were then seeded and perfused post-printing, followed by sequential brain microvascular endothelial cells (HBMECs) seeding. Both models were subjected to a six-day culture timeline and a 9-day endpoint. The 2.5D static culture conditions were utilized as a high-throughput screening platform for BBB tri-culture conditions with the 3D printed hydrogel, with the lead conditions being translated to a 3D tri-culture BBB model for therapeutic approaches under perfusion culture.

Determination of co-culture parameters in a step-wise approach using a 2.5D half-pipe hemi-cylinder model

To establish this BBB model, screening studies were performed using a printed hydrogel half-pipe model (Fig. 2a and b). This model enables the seeding of cells in a chamber containing a hemi-cylinder. The morphology of the cells in the curved region can be easily seen when using fluorescent cells such as GFP HBMECs (Fig. 2c). First, an endothelial barrier was established by seeding HBMECs into the channel of the half-pipe model and culturing with various cell culture media to determine optimal culturing conditions. One parameter that needed to be determined for the model was the type of media. In doing this, three types of media were examined: complete Vasculife media supplemented with 1% penicillin/streptomycin from Lifeline Cell Technologies, human brain microvascular endothelial cell media from Angio-Proteomie, and human brain microvascular pericyte media from Angio-Proteomie. VE-Cadherin immunostaining was conducted on half pipes after three days of culture for the HBMECs (Fig. 2d). With the VE-Cadherin immunostaining on the 2.5D half pipes, there is a clear result that Vasculife is the superior media to use for this model. The endothelial cells grown in Vasculife media display clearly defined cell–cell junctions that have thick bands surrounding the peripheries of the cells and a low amount of intracellular VE-Cadherin (Fig. 2d, left). In contrast, the endothelial cells grown on the 2.5D half pipes in HBMEC and HBMP media (Fig. 2d, center & d, right) display a higher amount of VE-Cadherin signal intracellularly, more jagged VE-Cadherin morphology, and notable gaps within the endothelial monolayer, indicated by the blue arrows.

Once Vasculife was decided as the media type to use for co-cultures, pericytes were incorporated with endothelial cells to determine additional parameters for their co-culture, specifically the timeline for culture and the ratio of endothelial cells to pericytes. The next parameter explored was the selection of timing for cell placement. Two strategies were employed: simultaneous seeding and sequential seeding. To replicate the seeding density used in the 3D channels of past,[24] an equivalent surface density of 0.4×10^6 cells cm^{-2} was held constant for the GFP HBMECs in all studies. In the simultaneous seeding, the GFP endothelial cells and RFP pericytes were mixed and seeded onto the half pipe as a mixture of the two cell types. For the sequential seeding, the pericytes were seeded onto the half-pipe and cultured for three days before the addition of endothelial cells. After three days of endothelial cell culture, varying morphologies are observed between the two routes of timing (Fig. 2e). For the simultaneous seeding, we see a disruption of the endothelial layer. In this disruption, rather than the two cell types co-existing in the same location, they take on a mosaic-like arrangement with patches of pericytes and patches of endothelial cells. This arrangement is not ideal as the endothelium is not able to provide the necessary barrier while there are large gaps in the monolayer. In contrast, for the half pipes that were seeded using a sequential strategy, we see both the endothelial cells and pericytes covering the entirety of the half pipe without any apparent gaps. It is hypothesized that the additional time given for pericyte attachment and stabilization before adding the endothelial cells may have enabled the formation of proper contacts for the endothelial cell-pericyte interaction.
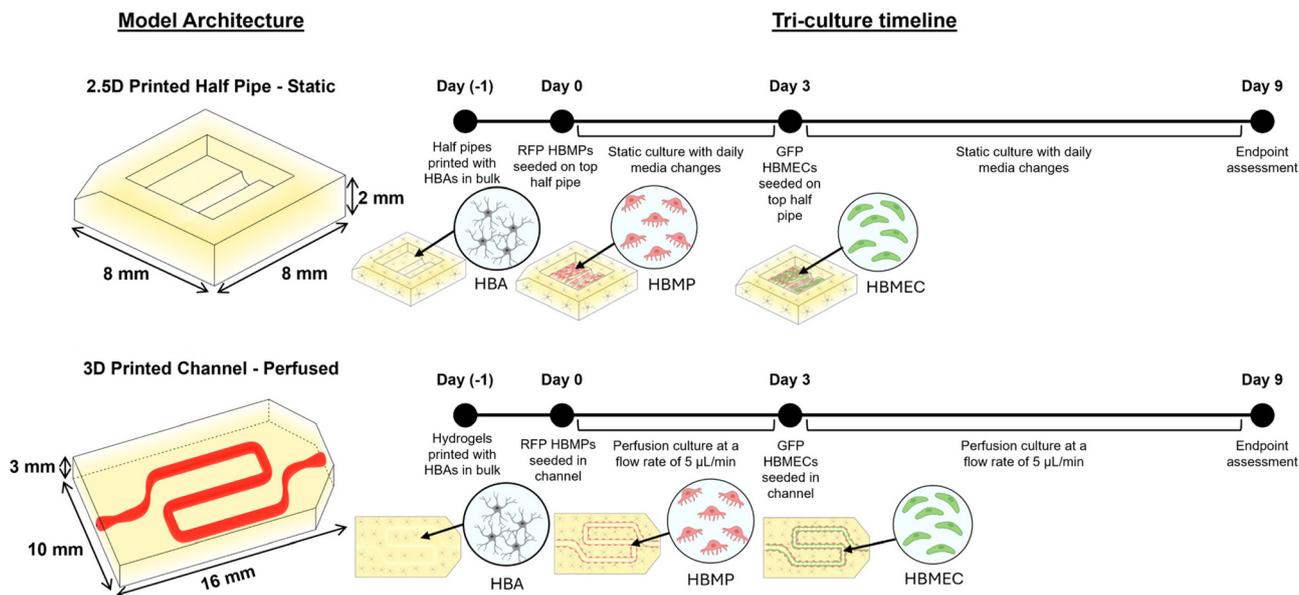
Fig. 1 Static and perfusion-based 3D printed models for BBB tri-culture structure and timeline. Static cultures were performed in 2.5D printed half pipe models and perfusion-based cultures were performed in a 3D printed serpentine channel model. Tri-cultures are present in both models, consisting of human brain astrocytes (HBA), RFP labelled human brain microvascular pericytes (RFP HBMP), and GFP labelled human brain microvascular endothelial cells (HBMEC).

Additionally, the extra time for the pericyte culture may have enabled the production and deposition of basement membrane proteins, which would also aid in endothelial adhesion and retention.

Next, this work sought to evaluate the ratio of pericytes to endothelial cells for the simultaneously seeded half pipes. The seeding density of pericytes was varied between $0.04–0.4 \times 10^6$ cells per cm^{-2} to mimic ratios of 10 : 1 to 1 : 1 endothelial cells to pericytes that are reported in the literature. There are various ratios of endothelial cells to pericytes found in the literature for *in vitro* models. Two frequently cited *in vitro* BBB models demonstrate a 10 : 1 ratio of endothelial cells to pericyte[20] and another showing a 5 : 1 ratio of endothelial cells to pericytes.[18] The CNS is generally regarded as having the highest pericyte coverage, and is reported to be between a 3 : 1 and a 1 : 1 endothelial-to-pericyte ratio.[27] Pericyte density and coverage are reported to positively correlate with endothelial barrier properties, so organs that have a more restrictive endothelium, specifically the brain, generally have a higher pericyte coverage.[28] Given this, the endothelial-to-pericyte ratios selected for these studies were 10 : 1, 6 : 1, 3 : 1, and 1 : 1, chosen to closely match those used in other *in vitro* models, as well as mimic the ratios reported for *in vivo* pericyte coverage. In addition to the co-culture ratios, endothelial-only and pericyte-only controls were also employed.

In doing this, pericytes were seeded on half pipes and cultured for three days before the addition of endothelial cells. After endothelial cells were added, the construct was cultured for an additional six days (a total of nine days of culture time). On the final day of culture, an interesting trend is seen across the varying ratio conditions (Fig. 2f). In both the pericyte-only and endothelial cell-only controls, the cells fill the entire length of the pipe. However, in all co-culture ratio conditions, it appears that the co-culture cell layer begins to retract from the edges of the pipe. Interestingly, it appears that both cells are detaching from the pipe surface and beginning to pull inwards towards the center of the pipe. This retraction from the sides of the half pipe is most notable in the conditions where there is a lower ratio of pericytes, specifically the 10 : 1 and 6 : 1 condition. The conditions that had a higher ratio of pericytes (1 : 1 and 3 : 1) still displayed some detachment and retraction of the cell layer. However, it was less substantial than the lower ratio conditions. The CNS has the highest pericyte to endothelial coverage throughout the body, so it is possible for these brain-specific cells that a ratio mimicking *in vivo* conditions is essential for proper function. Given this, the 1 : 1 ratio condition was selected as the most optimal for use in this model and is used in the studies going forward.

Incorporation of astrocytes for the tri-culture 2.5D model

After the optimal co-culture ratio conditions of endothelial cells and pericytes were determined, the next step was to move towards incorporating the third and final cell type to achieve the blood–brain barrier tri-culture: astrocytes. Astrocytes are located in the extracellular matrix surrounding blood vessels. To replicate this arrangement of cells, the integration of astrocytes in this model was accomplished by incorporating astrocytes into the print solution. Human brain astrocytes (HBAs) were printed into the bulk of the hydrogel at a concentration of 6×10^6 cells per mL. This concentration of astrocytes was selected as it has been previously demonstrated (unpublished work) that this concentration of cells can be included in the
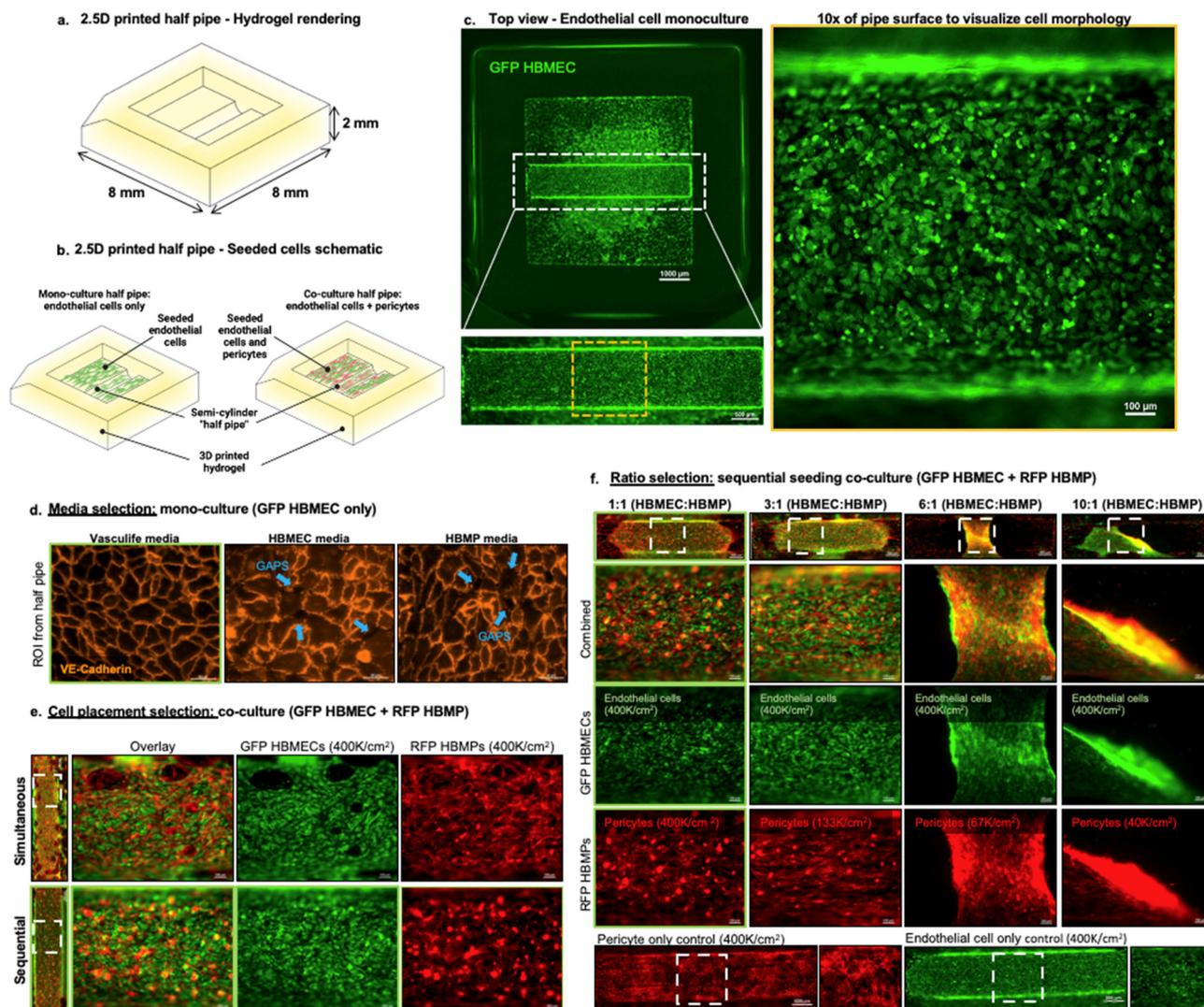
Fig. 2 Development of mono- and co-culture within this 3D printed hemi-cylinder model. (a–d) Mono-culture of endothelial cells only with justification for media type by immunostaining. (e and f) Co-culture of endothelial cells and pericytes with justification for seeding procedure and ratio selection (scale bar = 100 μm).

print solution and printed without the need for modifications to print parameters.

Once it was demonstrated that astrocytes could be printed into the bulk hydrogel, the studies progressed toward the incorporation of the pericytes and endothelial cells utilizing the optimized ratio. Hydrogel half pipes with astrocytes were printed and allowed to soak overnight before the next cell seeding. On day 0, the pericytes were seeded onto the half pipe at a density of 0.4×10^6 cells per cm^2, and there was homogenous coverage of pericytes across the pipe. After three days of culture, endothelial cells were seeded on top of the astrocyte-printed pericyte-laden half pipes. These tri-culture half pipes were cultured for an additional six days for a total of nine days of culture (Fig. 3a). From these images, the endothelial and pericyte layer is retained along the surface of the half-pipe for the entire duration of the experi-

ment, where the two cells co-exist in the same areas rather than forming gaps in one cell layer. Additionally, the endothelial layer begins to take on a more monolayer-like morphology by day six overall (day 3 endothelial cell culture). Pericytes also have a notable morphology progression over the tri-culture duration. Between days 0 and 3, the pericytes spread out along the surface of the half pipe. Their elongation and covering of the pipe continued for the remainder of the tri-culture timeline.

With the fabrication of this tri-culture using the printed half-pipe design, it was also important to assess the presence of cell–cell junctions within the model. To do this, the half pipe was immunostained for VE-Cadherin, and the presence and morphology of cell–cell junctions were analyzed. A 3D rendering of the half pipe immunostained for VE-Cadherin is shown from the side view and the top view (Fig. 3b, ESI
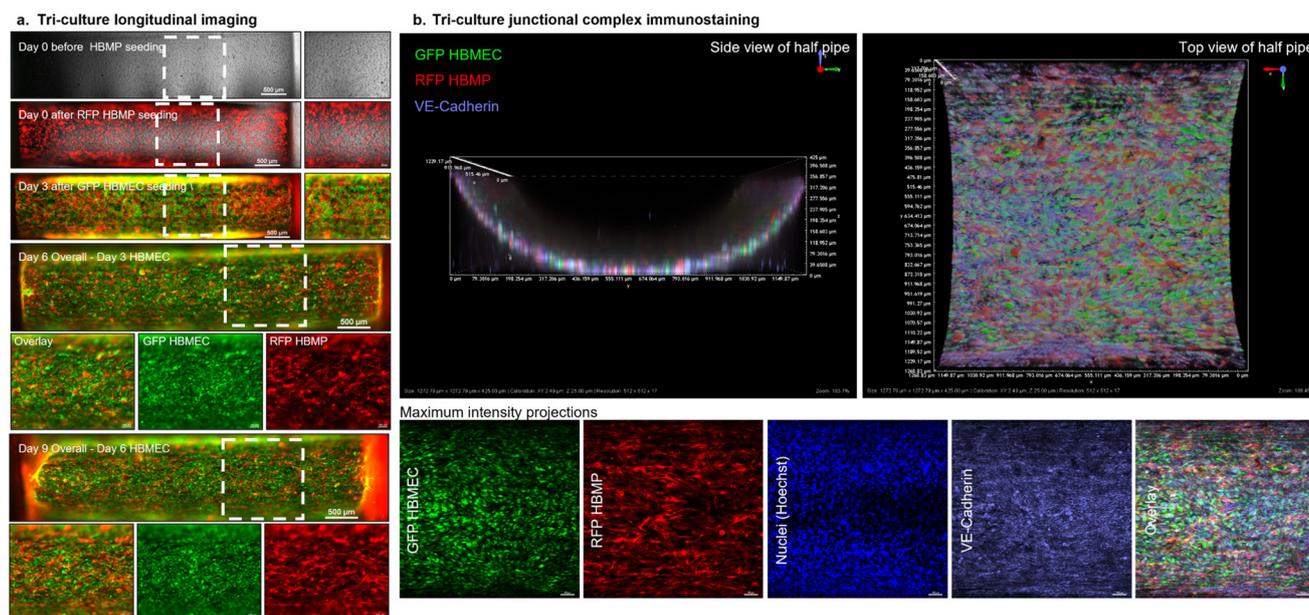
Fig. 3 Incorporation of astrocytes into the model for a 2.5D printed tri-culture model. (a) Tri-culture of endothelial cells, pericytes, and astrocytes with astrocytes printed into the bulk and imaged over the course of 9 days. Whole channel images (top) present hydrogel at each time point with white boxes to refer to the magnified areas of the corresponding figure (below). (b) After 9 days of culture, the tri-culture half pipe model was immunostained for VE-Cadherin (scale bar = 100 μm).

Fig. 2†), with maximum intensity projections for each channel shown below. From this, the presence of mature cell–cell junctions is demonstrated in this 2.5D tri-culture model.

Validation of the presence of blood–brain barrier efflux transporters and receptor-mediated transporters in the hemi-cylinder model

The blood–brain barrier (BBB) is a barrier that separates and restricts transport between the bloodstream and the extracellular space of the brain. Maintenance of brain homeostasis is ensured by the presence and organization of tight junctions, as well as the existence of transporters.[28,29] In developing an *in vitro* BBB model, it is imperative that the model display the presence of BBB transporters, demonstrating sufficient complexity for use as an *in vitro* screening tool.

P-glycoprotein (P-gp) is a prominent BBB endothelial efflux transporter in the ABCB family, which plays a role in the transport of several compounds across the BBB. P-gp is located throughout the body in organs and tissues with either excretory functions (such as the liver, kidney, and small intestine), as well as those with BBB (such as the blood-testis barrier and placenta).[30,31] P-gp is essential for maintaining brain homeostasis and ensuring harmful compounds in the bloodstream do not cross over into brain tissue. However, it can also pose a challenge for delivering therapeutics from the bloodstream across the BBB. This is a result of P-gp expelling compounds back into the bloodstream once they enter the cell membrane. As a result, many therapeutic strategies have aimed to inhibit P-gp expression to enable the transport of therapeutics across the blood–brain barrier.[32]

In this model, the presence of P-gp was confirmed with immunostaining on the 2.5D half-pipe, as seen in Fig. 4a. Demonstrating the presence of this efflux transporter within the hydrogel model displays sufficient complexity for use as a screening tool to assess therapeutic strategies that operate *via* P-gp inhibition. While immunostaining confirms the presence of these transporters, future studies may employ functional assays to confirm that these transporters are functioning as expected under the culture conditions. One area where P-gp inhibition is used as a tool is to deliver anticancer drugs. P-gp in the BBB restricts the entry of many anticancer drugs from the bloodstream to the brain. Inhibition of this efflux transporter has shown promise in delivering anticancer drugs to brain tumors *via* the co-administration of anticancer drugs and a P-gp inhibitor.[33] In the translation to the 3D printed perfusable hydrogel model, this delivery route could be studied *via* the perfusion of an anticancer compound with a P-gp inhibitor and quantifying the amount of anticancer compound that has crossed the cellular barrier.

The next transporter assessed in this model was the breast cancer resistance protein (BCRP). BCRP, like P-gp, is a drug efflux ABC transporter principally expressed on the luminal membrane of brain endothelial cells. It has been demonstrated within the human blood–brain barrier that P-gp and BCRP are the central ABC transporter genes expressed in brain microvessels.[34] As a result, many efflux pump inhibition strategies focus on P-gp and BCRP. In the model displayed here, the presence of the efflux transporter, BCRP, is confirmed *via* the use of immunostaining (Fig. 4b). This, taken together with the presence of P-gp, demonstrates that this model could be suitable for utility in screening therapeutic strategies that work *via* efflux pump inhibition.
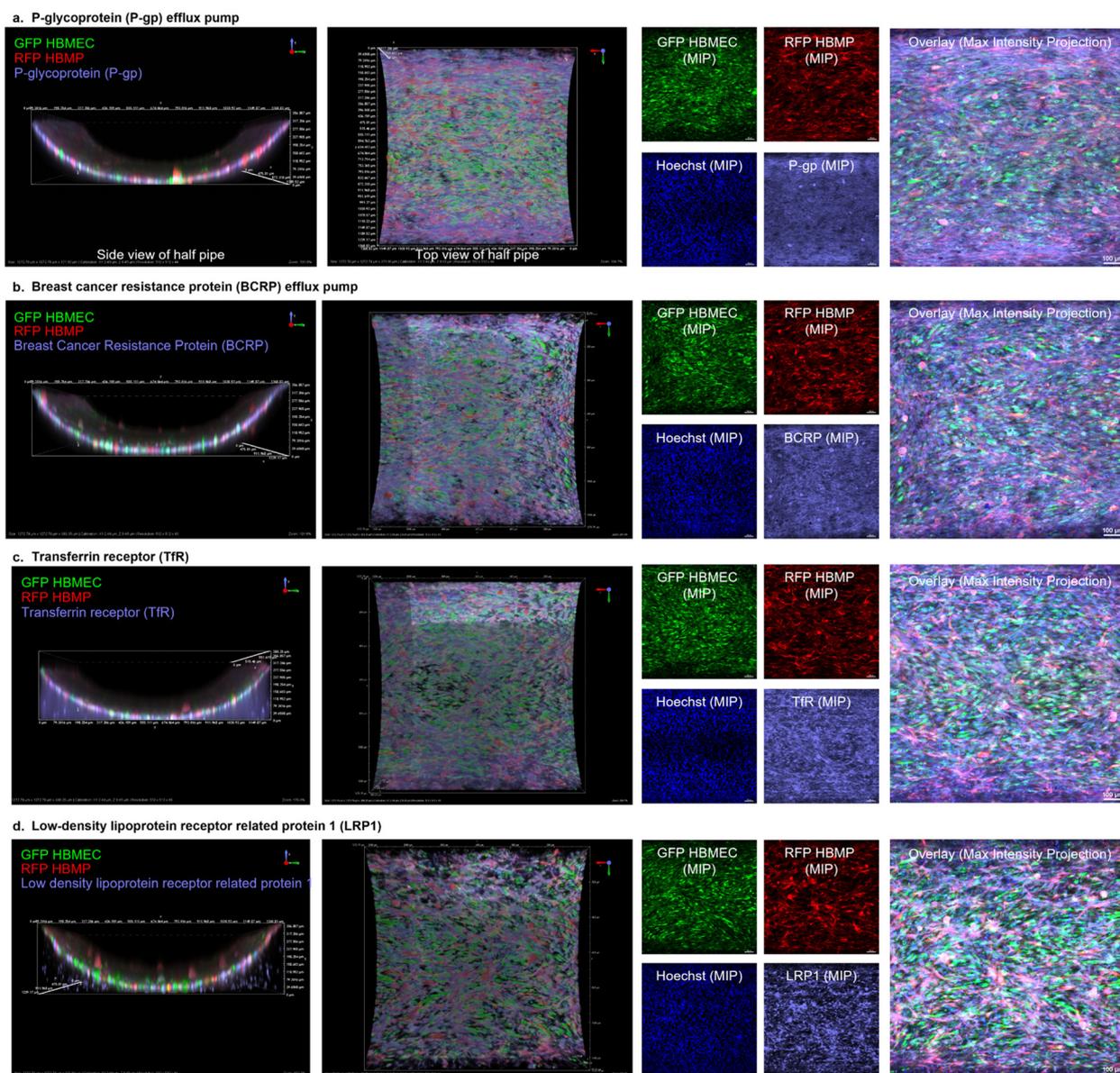
Fig. 4 Immunostaining of crucial blood-brain barrier transporters. (a) P-glycoprotein (P-gp) immunostaining. Side view of tri-culture hydrogel half pipe immunostained for P-glycoprotein on day 9 of culture. 3D renderings show GFP HBMECs (green), RFP HBMPs (red), and P-glycoprotein (purple). Top view of tri-culture. Maximum intensity projections of a confocal z-stack going through the entire z-dimension of the half pipe from the base of the pipe to the top of the hemi-cylinder channel sides (z dimension ~400 μm). Individual channels of the maximum intensity projections shown are GFP HBMEC (488nm laser), RFP HBMP (560nm laser), Hoechst (405nm laser), and P-glycoprotein (647nm laser). (b) Breast cancer resistance protein (BCRP). (c) Transferrin receptor (TfR). (d) Low-density lipoprotein receptor related protein 1 (LRP1) (scale bar = 100 μm).

The next transporter that was assessed was the transferrin receptor. Brain capillary endothelial cells have several unique properties, one being that these cells express receptors and transporters that play a role in the uptake of molecules from the bloodstream. These transporters transport biologics to the brain parenchyma *via* receptor-mediated transport. Due to the strong tight junctions between brain endothelial cells, alternative routes must be devised for delivering therapeutic proteins with high molecular weight to the brain. One route to deliver such large molecules utilizes receptor-mediated transport.

Receptor-mediated transport is an exciting route to explore for drug delivery, as it enables the transport of large molecule drugs across the blood–brain barrier. One prevalent method that is used for receptor-mediated transport is the use of antibodies against the transferrin receptor. Iron is essential to the brain's cells, so the endothelial cells contain a special mechanism to ensure iron transport across their restrictive barrier. The iron in blood serum is complexed with the iron-binding protein transferrin. Transferrin is a glycoprotein whose primary function is the transport of iron throughout the body, as iron cannot travel by itself. When the complex of iron and

transferrin reaches a transferrin receptor (TfR), the transferrin with iron binds to the receptor, and endocytosis occurs, forming a vesicle that carries the bound transferrin and iron into the cell.[35]

One strategy used for brain delivery of high molecular weight therapeutic proteins is the molecular Trojan horse (MTH) method, which delivers therapeutic proteins into the brain *via* receptor-mediated endocytosis and transcytosis. The insulin receptor and the transferrin receptor are the most common receptors expressed on the luminal side of brain endothelial cells that are used for the molecular Trojan horse method.[36] In this method, a therapeutic protein drug is fused to an antibody that binds to a specific receptor on the endothelial cells of the BBB. This approach enables the receptor-mediated delivery of the fusion protein across the restrictive BBB and delivers the therapeutic protein to the brain.[37] In this model, the presence of the transferrin receptor was confirmed with immunostaining on the 2.5D half pipe, as seen in Fig. 4c. This shows promise that this model can be used as an *in vitro* screening tool for therapeutic strategies that operate *via* the molecular Trojan horse method to deliver large molecule therapeutics.

The final transporter assessed in this model was low-density lipoprotein receptor-related protein 1 (LRP1). Similar to the drug delivery approach utilizing the transferrin receptor, delivery approaches involving LRP1 also rely on receptor-mediated transcytosis, taking advantage of the highly expressed endogenous receptors and mechanisms present at the endothelial cells of brain capillaries. Due to the extensive capillary network and perfusion rate within the brain, using transporters for receptor-mediated transport is considered one of the most effective methods to deliver therapeutic drugs to the brain parenchyma and is recognized as one of the methods with the most likely chance of success.[38]

There are several receptors in the low-density lipoprotein receptor (LDLR) family; however, LRP1 is the most studied receptor within this family due to its critical role in multiple pathways in the pathogenesis of Alzheimer's Disease.[39] Within the last decade, evidence has emerged that suggests that LRP1 is involved in regulating the brain and systemic clearance of Alzheimer's disease amyloid β-peptide (Aβ) *via* transcytosis through the brain endothelium for systemic elimination, and it has been suggested that impairment of LRP1 contributes to the accumulation of amyloid-β and drives Alzheimer's disease pathology. LRP1 has roles in both the generation and clearance of amyloid-β; the endocytosis of amyloid precursor protein (mediated by LRP1) is necessary for the generation of amyloid-β within the cells; however, LRP1 is also involved in the clearance of extracellular amyloid-β.[40]

In addition to being involved in the pathology of Alzheimer's, understanding LRP1 and its transport mechanism is also of interest for other pathologies, such as brain tumors like glioblastoma. Glioblastoma is extremely difficult to treat, one reason being the presence of restrictive barriers such as the blood–brain barrier and the blood–brain tumor barrier, thus underscoring the need for drug delivery strat-

egies. LRP1 is widely expressed in the BBB, as well as in glioblastoma. One of the ligands that LRP1 interacts with, receptor-associated protein (RAP), can bind to LRP1 and internalize into the endothelial cells with these receptors *via* receptor-mediated transport. Additionally, receptor-associated protein has been shown to cross the BBB more efficiently than transferrin, demonstrating promise as an effective brain delivery tool.[41] The presence of LRP1 in this hydrogel model, seen in Fig. 4d, demonstrates that this *in vitro* model can be used as a screening tool to study drug delivery approaches and pathologies associated with the LRP1 transporter. Altogether, the 2.5D static culture model demonstrates presence of BBB transport proteins (Fig. 4, ESI Fig. 3 and video 1†), and therefore allows for further high throughput investigation of transport proteins that are essential to the function of the BBB.

Demonstration of therapeutic screening capabilities under ultrasound application

In pilot studies, we demonstrated the fabrication of the optimized BBB tri-culture model in the perfused serpentine architecture (Fig. 5a and b). Furthermore, we evaluated the cross-section of the tri-culture BBB model to identify astrocyte proximity to the open perfusable channel, which revealed elongated astrocyte endfeet towards the cellularized channels with optimized HBMP and HBMECs condition (Fig. 5c). We then assessed the transport of a model compound perfused through the vasculature under ultrasound (Fig. 5d). These studies leveraged a rapidly growing new class of drugs, fluorescently conjugated Immunoglobulin G (IgG), to represent therapeutic antibodies. The perfusate consisting of IgG-AlexaFluor-555 and microbubbles to serve as the molecular tracer and agent for sonoporation, respectively, was perfused through the channel, and ultrasound was applied. Timelapse acquisitions during the ultrasound-permeability trial enabled the assessment of cell morphology and rearrangement during the ultrasound (ESI video 2†). Before ultrasound, a substantial number of endothelial cells and pericytes were present in the channel, and the endothelial cells appeared to be interdigitating. However, as ultrasound was applied, the cells began to rearrange and shift (Fig. 5d). The ultrasound-permeability GUI developed previously[25] was used to quantify vascular permeability before and after ultrasound application in this tri-culture model, and there was a substantial increase in the vascular permeability coefficient after ultrasound application (Fig. 5e, bottom). The average permeability of the tri-culture gels before ultrasound was $0.24\ e^{-6}$ cm s^{-1}, while the average permeability of the tri-culture gels after ultrasound was $0.83\ e^{-6}$ cm s^{-1}, demonstrating that the use of ultrasound and microbubbles played a role in enhancing transport of the conjugated antibody across the engineered blood–brain barrier of this model. Consistent with previously reported values ranging from $1–2\ e^{-6}$ cm s^{-1} for non-specific CNS drugs within *in vitro* and *in vivo* systems.[42] While the tri-culture model demonstrates a promising application, further investigation into efflux transporters and the transport of bioactive agents will be
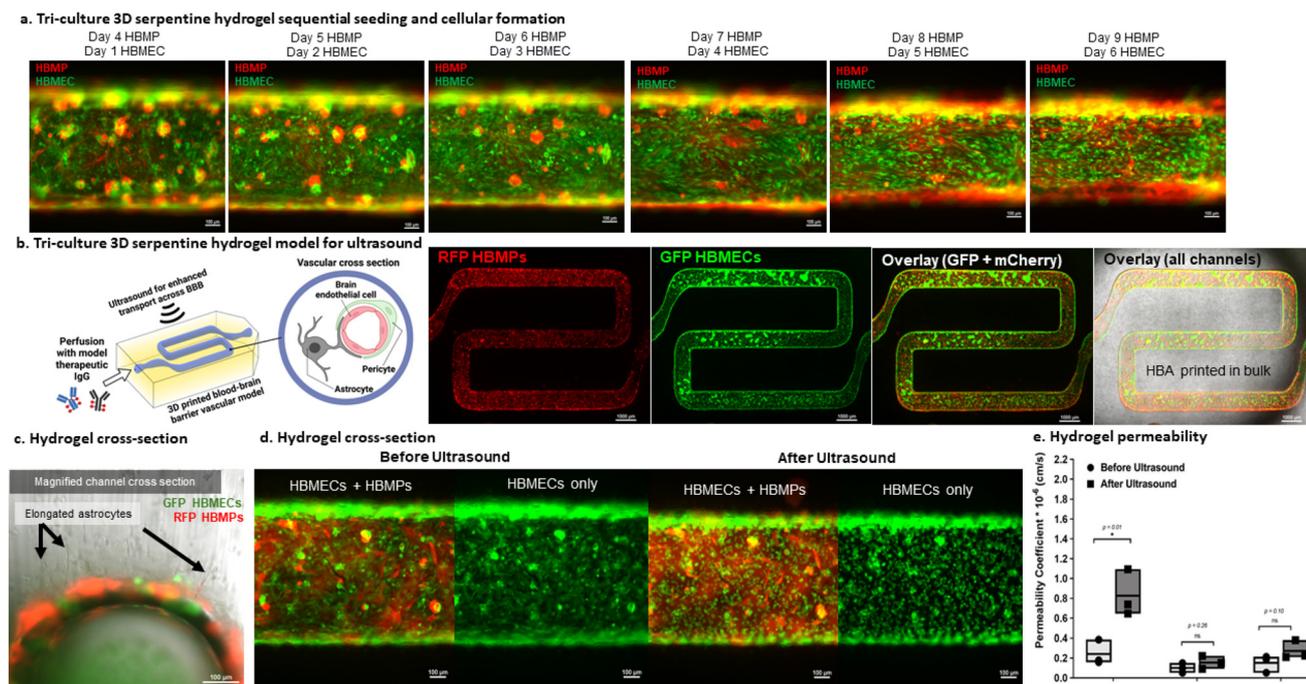
Fig. 5 Demonstration of therapeutic screening capabilities with this 3D printed tri-culture *in vitro* BBB model. (a) Tri-culture serpentine hydrogel model after being printed with astrocytes at 6×10^6 cells per mL, seeded with 30×10^6 cells per mL RFP HBMP on day 0, and seeded again with 30×10^6 cells per mL GFP HBMEC and imaged for barrier formation (scale bar = 100 μm). (b) Construct perfused with Vasculife media at 5 μL min^{-1} prior to ultrasound-permeability studies on day 3 (scale bar = 1000 μm). (c) Hydrogel cross-section of bulk area with visible astrocyte endfeet near channel with seeded RFP HBMP and GFP HBMECs (scale bar = 100 μm). (d) Images from the center serpentine channel where the permeability acquisition was acquired before IgG-AF555 was perfused through the channel under ultrasound application and after (scale bar = 100 μm). (e) Vascular permeability coefficient before and after ultrasound for three tri-culture gels, astrocyte only hydrogels, and acellular hydrogels. Floating bars go from the minimum to the maximum of the data set with a line at the mean. Significance was determined by analyzing the before and after permeability values of the same group using a paired *t*-test (**p* < 0.05).

necessary for further development of the 3D BBB tri-culture model.

Currently, transwell or Boyden chamber assays such as transendothelial electrical resistance (TEER) and molecular tracer permeability are used for assessing endothelial barrier functionality.[43–48] However, these models rely on monolayer culture systems, or possess cells in different compartments rather than interacting directly with one another, lack real time tracking of barrier integrity, and most importantly they do not account for shear stress on the barrier function.[49–53] We have previously established the use of 3D bioprinting to fabricate models that possess a cell barrier to elucidate vascular permeability for ultrasound-assisted delivery of therapeutics.[24] This technology allows real time evaluation of a cell barrier, allows cells to interact with one another to resemble more closely that of the native environment, and can be modified to incorporate shear stress. Here, we showcase this 3D bioprinting technology for more specific applications such as the BBB. Future studies will utilize these findings described here for a BBB model that can either be a 2.5D that could eventually be modified for the incorporation of electrodes to further investigate BBB mechanisms or a 3D perfusable platform to investigate shear stress and the impact of a perfusable microenvironment on drug delivery to the BBB. Overall, these

models show exciting promise as platforms that could be used in the late stages of drug discovery or the early stages of preclinical drug development for assessing the ability of compounds to traverse the BBB in treating neurological conditions.

Conclusion

In summary, this work has established a 3D printable hydrogel blood–brain barrier model with relevant cell populations and organization and has demonstrated the potential for evaluating transport across this restrictive barrier *in vitro*. The 2.5D static hydrogel half pipe provided an efficient method to determine tri-culture parameters in a resource-conservative and high-throughput manner. Translating these parameters to a 3D-perfusable model enables studying transport under controlled flow conditions in a more physiologically relevant setting. In contrast to existing assays, this *in vitro* model enables direct cell–cell contact between endothelial cells and the supporting cell populations of the blood–brain barrier, a crucial aspect in recapitulating the native environment. Additionally, the use of 3D printing enables the precise patterning of complex architectures and the ability to pattern

regions for the incorporation of additional cell types (cancer cell lines, disease model organoids, *etc.*) that would enable the fabrication of a more complex disease model where the treatment of diseased cells outside the BBB vasculature could be examined. The confirmation of efflux transporters (P-glycoprotein and breast cancer resistance protein), as well as receptor-mediated transporters (Transferrin receptor and low-density lipoprotein receptor-related protein-1), demonstrates that this model is suitable for assessing therapeutic drug delivery strategies whose mechanisms rely on these transporters such as efflux pump inhibition and therapeutic delivery *via* receptor-mediated transporters. Thus far, this 3D printable blood–brain barrier model has demonstrated exciting potential for use as a scalable screening platform to investigate transport across this restrictive barrier and has the potential to inform decisions about neurotherapeutic drug design and therapeutic strategies targeting the blood–brain barrier.

Data availibility

The data supporting this article have been included as part of the ESI.†

Conflicts of interest

Y.H., N.B., J.X., and A.T.P. are employees of Merck Sharp & Dohme Corp., a subsidiary of Merck & Co., Inc., Rahway, NJ, USA, and may hold stock or stock options in Merck & Co., Inc., Rahway, NJ, USA.

Acknowledgements

References

1   C. Hajal, B. Le Roi, R. D. Kamm and B. M. Maoz, *Annu. Rev. Biomed. Eng.*, 2021, **23**, 359–384.
2   X. Chen, C. Liu, L. Muok, C. Zeng and Y. Li, *Cells*, 2021, 1–23.
3   A. M. Hopkins, E. DeSimone, K. Chwalek and D. L. Kaplan, *Prog. Neurobiol.*, 2015, **125**, 1–25.
4   M. W. van der Helm, A. D. van der Meer, J. C. T. Eijkel, A. van den Berg and L. I. Segerink, *Tissue Barriers*, 2016, **4**, DOI: **10.1080/21688370.2016.1142493**.
5   K. J. Jang, M. A. Otieno, J. Ronxhi, H. K. Lim, L. Ewart, K. R. Kodella, D. B. Petropolis, G. Kulkarni, J. E. Rubins, D. Conegliano, J. Nawroth, D. Simic, W. Lam, M. Singer, E. Barale, B. Singh, M. Sonee, A. J. Streeter, C. Manthey, B. Jones, A. Srivastava, L. C. Andersson, D. Williams, H. Park, R. Barrile, J. Sliz, A. Herland, S. Haney, K. Karalis,
       D. E. Ingber and G. A. Hamilton, *Sci. Transl. Med.*, 2019, **11**, 517.
6   S. Perrin, *Nature*, 2014, **507**, 423–425.
7   H. Kimura, Y. Sakai and T. Fujii, *Drug Metab. Pharmacokinet.*, 2018, **33**, 43–48.
8   J. J. Han, *Artif. Organs*, 2023, **47**, 449–450.
9   S. A. Dugger, A. Platt and D. B. Goldstein, *Nat. Rev. Drug Discovery*, 2018, **17**, 183–196.
10 C. Ma, Y. Peng, H. Li and W. Chen, *Trends Pharmacol. Sci.*, 2021, **42**, 119–133.
11 D. Huh, B.D. Matthews, A. Mammoto, M. Montoya-Zavala, H.Y. Hsin and D.E. Ingber, *Science*, 2010, **328**, 1662–1668.
12 V. Allwardt, A. J. Ainscough, P. Viswanathan, S. D. Sherrod, J. A. McLean, M. Haddrick and V. Pensabene, *Bioengineering*, 2020, **7**, 1–27.
13 N. R. Wevers, D. G. Kasi, T. Gray, K. J. Wilschut, B. Smith, R. Vught, F. Shimizu, Y. Sano, T. Kanda, G. Marsh, S. J. Trietsch, P. Vulto, H. L. Lanz and B. Obermeier, *Fluids Barriers CNS*, 2018, **15**, 1–12.
14 C. A. Dessalles, C. Leclech, A. Castagnino and A. I. Barakat, *Commun. Biol.*, 2021, **4**, 764.
15 A. Herland, A. D. Van Der Meer, E. A. FitzGerald, T. E. Park, J. J. F. Sleeboom and D. E. Ingber, *PLoS One*, 2016, **11**, e0150360.
16 P. P. Partyka, G. A. Godsey, J. R. Galie, M. C. Kosciuk, N. K. Acharya, R. G. Nagele and P. A. Galie, *Biomaterials*, 2017, **115**, 30–39.
17 J. A. Kim, H. N. Kim, S. K. Im, S. Chung, J. Y. Kang and N. Choi, *Biomicrofluidics*, 2015, **9**, 024115.
18 S. Seo, S. Nah, K. Lee, N. Choi and H. N. Kim, *Adv. Funct. Mater.*, 2021, **2106860**, 2106860.
19 E. Urich, C. Patsch, S. Aigner, M. Graf, R. Iacone and P. O. Freskgård, *Sci. Rep.*, 2013, **3**, 1500.
20 C. Hajal, G. S. Offeddu, Y. Shin, S. Zhang, O. Morozova, D. Hickman, C. G. Knutson and R. D. Kamm, *Nat. Protoc.*, 2021, **2022**, 1–34.
21 M. Campisi, Y. Shin, T. Osaki, C. Hajal, V. Chiono and R. D. Kamm, *Biomaterials*, 2018, **180**, 117–129.
22 A. Marino, O. Tricinci, M. Battaglini, C. Filippeschi, V. Mattoli, E. Sinibaldi and G. Ciofani, *Small*, 2018, **14**(6), DOI: **10.1002/SMLL.201702959**.
23 H. Yue, K. Xie, X. Ji, B. Xu, C. Wang and P. Shi, *Biomaterials*, 2020, **245**, 119980.
24 M. K. Royse, A. K. Means, G. A. Calderon, I. S. Kinstlinger, Y. He, M. R. Durante, A. T. Procopio, O. Veiseh and J. Xu, *Biomater. Sci.*, 2022, 16–21.
25 B. Grigoryan, S. J. Paulsen, D. C. Corbett, D. W. Sazer, C. L. Fortin, A. J. Zaita, P. T. Greenfield, N. J. Calafat, J. P. Gounley, A. H. Ta, F. Johansson, A. Randles, J. E. Rosenkrantz, J. D. Louis-Rosenberg, P. A. Galie, K. R. Stevens and J. S. Miller, *Science*, 2019, **364**, 458–464.
26 I. S. Kinstlinger, G. A. Calderon, M. K. Royse, A. K. Means, B. Grigoryan and J. S. Miller, *Nat. Protoc.*, 2021, 3089–3113.
27 T. M. Mathiisen, K. P. Lehre, N. C. Danbolt and O. P. Ottersen, *Glia*, 2010, **58**, 1094–1103.

28 L. Diaz-Flores, R. Gutierrez, H. Varela, N. Rancel and F. Valladares, *Histol. Histopathol.*, 1991, **6**, 269–286.

29 M. Piantino, D.-H. Kang, T. Furihata, N. Nakatani, K. Kitamura, Y. Shigemoto-Mogami, K. Sato and M. Matsusaki, *Mater. Today Bio*, 2022, **15**, 100324.

30 M. F. Fromm, *Trends Pharmacol. Sci.*, 2004, **25**, 423–429.

31 M. Aryal, K. Fischer, C. Gentile, S. Gitto, Y. Z. Zhang and N. McDannold, *PLoS One*, 2017, **12**, e0166061.

32 F. Mo, A. Pellerino, R. Soffietti and R. Rudà, *Int. J. Mol. Sci.*, 2021, **22**, 12654.

33 E. M. Kemper, W. Boogerd, I. Thuis, J. H. Beijnen and O. van Tellingen, *Cancer Treat. Rev.*, 2004, **30**, 415–423.

34 S. Dauchy, F. Dutheil, R. J. Weaver, F. Chassoux, C. Daumas-Duport, P. O. Couraud, J. M. Scherrmann, I. De Waziers and X. Declèves, *J. Neurochem.*, 2008, **107**, 1518–1528.

35 E. Mills, X. P. Dong, F. Wang and H. Xu, *Future Med. Chem.*, 2010, **2**, 51–64.

36 G. Xiao and L. S. Gan, *Int. J. Cell Biol.*, 2013, 703545.

37 W. M. Pardridge, *Curr. Opin. Pharmacol.*, 2006, **6**, 494–500.

38 R. Gabathuler, *Neurobiol. Dis.*, 2010, **37**, 48–57.

39 T. Kanekiyo and G. Bu, *Front. Aging Neurosci.*, 2014, **6**, 93.

40 S. E. Storck and C. U. Pietrzik, *Pharm. Res.*, 2017, **34**, 2637–2651.

41 H. Ruan, Z. Chai, Q. Shen, X. Chen, B. Su, C. Xie, C. Zhan, S. Yao, H. Wang, M. Zhang, M. Ying and W. Lu, *J. Controlled Release*, 2018, **279**, 306–315.

42 G. Le Roux, R. Jarray, A. Guyot, S. Pavoni, N. Costa, F. Theodoro, F. Nassor, A. Pruvost, N. Tournier, Y. Kiyan, O. Langer, F. Yates, J. Deslys and A. Mabondzo, *Sci. Rep.*, 2019, **9**, 16310.

43 J. Xu, S. S. Y. Lee, H. Seo, L. Pang, Y. Jun, R. Y. Zhang, Z. Y. Zhang, P. Kim, W. Lee, S. J. Kron and Y. Yeo, *Small*, 2018, **14**, 1–16.

44 H. M. Lander, A. M. Grant, T. Albrecht, T. Hill and C. J. Peters, *Am. J. Trop. Med. Hyg.*, 2014, **90**, 993.

45 K. Miyazaki, K. Hashimoto, M. Sato, M. Watanabe, N. Tomikawa, S. Kanno, Y. Kawasaki, N. Momoi and M. Hosoya, *Pediatr. Res.*, 2017, **81**, 942–994.

46 Y. Wang and J. S. Alexander, *Methods Mol. Biol.*, 2011, **763**, 253–264.

47 I. Bischoff, M. C. Hornburger, B. A. Mayer, A. Beyerle, J. Wegener and R. Fürst, *Sci. Rep.*, 2016, **6**, 1–11.

48 J. Wegener and J. Seebach, *Cell Tissue Res.*, 2014, **355**, 485–514.

49 D. Mehta and A. B. Malik, *Physiol. Rev.*, 2006, **86**, 279–367.

50 D. E. Berardi and J. M. Tarbell, *Cell. Mol. Bioeng.*, 2009, **2**, 320–331.

51 G. M. Price, K. H. K. Wong, J. G. Truslow, A. D. Leung, C. Acharya and J. Tien, *Biomaterials*, 2010, **31**, 6182–6189.

52 O. C. Colgan, G. Ferguson, N. T. Collins, R. P. Murphy, G. Meade, P. A. Cahill and P. M. Cummins, *Am. J. Physiol.: Heart Circ. Physiol.*, 2007, **292**, 3190–3197.

53 J. M. Tarbell, *Cardiovasc. Res.*, 2010, **87**, 320–330.